Enhanced Heat Transfer in Biporous Wicks in the Thin Liquid Film Evaporation and Boiling Regimes

Dušan Ćoso

Vinod Srinivasan

Department of Mechanical Engineering,
University of California,
Berkeley, CA 94720-1740

Ming-Chang Lu

Department of Mechanical Engineering,
National Chiao Tung University,
Hsinchu, Taiwan 30010

Je-Young Chang

Intel Corporation,
5000 W. Chandler Boulevard, CH5-157,
Chandler, AZ 85226

Arun Majumdar

Advanced Research Projects
Agency-Energy (ARPA-E),
US Department of Energy,
Washington, D.C. 20585
e-mail: Arun.Majumdar@hq.doe.gov

Biporous media consisting of microscale pin fins separated by microchannels are examined as candidate structures for the evaporator wick of a vapor chamber heat pipe. The structures are fabricated out of silicon using standard lithography and etching techniques. Pores which separate microscale pin fins are used to generate high capillary suction, while larger microchannels are used to reduce overall flow resistance. The heat transfer coefficient is found to depend on the area coverage of a liquid film with thickness on the order of a few microns near the meniscus of the triple phase contact line. We manipulate the area coverage and film thickness by varying the surface area-to-volume ratio through the use of microstructuring. Experiments are conducted for a heater area of 1 cm² with the wick in a vertical orientation. Results are presented for structures with approximately same porosities, fixed microchannel widths w ≈ 30 µm and w ≈ 60 µm, and pin fin diameters ranging from d = 3–29 µm. The competing effects of increase in surface area due to microstructuring and the suppression of evaporation due to reduction in pore scale are explored. In some samples, a transition from evaporative heat transfer to nucleate boiling is observed. While it is difficult to identify when the transition occurs, one can identify regimes where evaporation dominates over nucleate boiling and vice versa. Heat transfer coefficients of 20.7 (±2.4) W/cm²-K are attained at heat fluxes of 119.6 (±4.2) W/cm² until the wick dries out in the evaporation dominated regime. In the nucleate boiling dominated regime, heat fluxes of 277.0 (±9.7) W/cm² can be dissipated by wicks with heaters of area 1 cm², while heat fluxes up to 733.1 (±103.4) W/cm² can be dissipated by wicks with smaller heaters intended to simulate local hot-spots. [DOI: 10.1115/1.4006106]

Keywords: biporous wick structure, heat transfer coefficient, dryout heat flux, hot-spot, heater area, evaporation, boiling

1 Introduction

The integration of graphical processing units with central processing units as well as the use of multicore processors can pose two severe challenges in thermal management, namely: (i) how to cool local hot-spots on the order of 1 mm in size with power densities exceeding 500 W/cm²; and (ii) how to dissipate more than 100 W over a chip area of about 1 cm², i.e., for average chip power densities exceeding 100 W/cm² [1,2]. Vapor chamber heat pipes have received attention for thermal management of these processor chips since they have a high heat transfer coefficient for heat spreading and require no external source of power or liquid pumping making them ideal for portable or handheld devices [3,4]. Ideally, a heat pipe spreader is designed such that it can dissipate a given heat flux while maintaining a minimal temperature rise. This heat dissipation capability depends significantly on the performance of the evaporator section of the heat pipe, which is typically composed of a porous wick.

In general, two factors restrict the operating envelope of a heat pipe, namely: (i) the capillary suction limited mass flow rate, and (ii) the initiation of nucleate boiling in the evaporator wick. Evaporator wicks are typically made of sintered copper particles. In these types of structures, the twin goals of increasing both the dissipated heat flux and the overall heat transfer coefficient are in

conflict [4]. Reduction of particle size and increase in wick thickness favor higher capillary driven mass flow rate, thus increasing the heat flux dissipated. However, particle size reduction also increases liquid flow resistance and the density of point contacts between particles thus reducing the effective thermal conductivity of the wick. These and other factors for the optimal design of porous wick structures have been examined in great detail by Faghri [5]. With these tradeoffs in mind, there is likely an optimum particle size, wick height, and wick porosity that maximize the heat transfer coefficient and the heat flux that can be dissipated.

During heat pipe operation, heat is conducted from the wick base through the particle matrix, and further into liquid toward the evaporating liquid–vapor interface. Due to the low conductivity of the liquid, most of the heat transfer at the top surface occurs in the liquid region (thickness ∼ few microns) near the triple-phase contact line [6–8]. The observed heat transfer coefficient is governed by the area coverage and thickness of this thin liquid film region, and the effective conductivity of the porous matrix [9]. Figure 1 shows an idealized sketch of the thermal resistance network of a sintered copper particle wick. Here, $R_{\text{substrate}}$ is the substrate thermal resistance on which the particles are sintered, R_{matrix} is the effective thermal resistance of the particle/liquid matrix, R_{film} is the thermal resistance of the thin liquid film that forms at the meniscus, and R_{int} is the thermal resistance of the liquid/vapor interface. Additionally, Q, T_{vap} T_{wall}, and $T_{\text{substrate}}$ are the heat flow, vapor temperature, temperature at the wall in contact with the liquid, and temperature at the base of the substrate respectively. Thus, given that the interfacial thermal resistance is not the
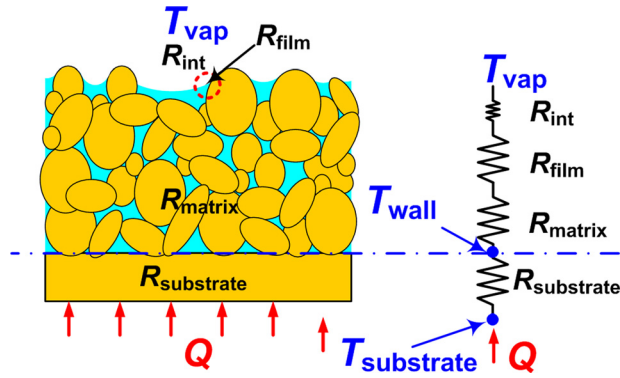

Fig. 1 Thermal resistance network for a typical sintered copper particle porous wick structure; Q is the applied power, T_{wall} is the temperature at the base of the particle matrix, $T_{substrate}$ is the temperature at the base of the wick substrate, $R_{substrate}$ the thermal resistance of the substrate, R_{matrix} is the overall thermal resistance of the particle/liquid matrix, R_{film} is the resistance of the liquid thin film that forms at the meniscus, R_{int} is the thermal resistance of the liquid/vapor interface, and T_{vap} is the vapor temperature

dominant resistance in such a system [5], one can tune other resistances to maximize wick performance. Wicks with sintered particles in the range 40–400 μm and typically of 1–4 mm thickness have been tested by several researchers [9–14]. The highest observed heat transfer coefficient in the evaporative regime of heat transfer using sintered particle wicks is 12.8 W/cm^2-K at an applied flux of 8.3 W/cm^2 [10]. All other wicks that display capillary evaporation show values in the range 1–10 W/cm^2-K.

In the past, biporous media consisting of large clusters of small particles have been shown to increase the heat dissipation capacity [11]. In these structures, the capillary suction is generated by the small pores inside the particle clusters while the viscous drag is reduced as a result of liquid flow through the large voids between the clusters, thereby extending the capillary limit. However, significant increases in evaporative heat transfer coefficient have not been demonstrated, presumably due to low solid thermal conductivity of such structures and thus a large thermal resistance of the liquid/particle matrix (R_{matrix}) as illustrated in Fig. 1. In other structures, nucleate boiling is observed at relatively low superheats, accompanied by high heat transfer coefficients [12–16]. Semenic et al. [12] use a wick consisting of large clusters of small copper particles and suggest that the small pores serve to transport liquid to the boiling sections by capillary suction, while large pores between the clusters facilitate vapor transport away from the wick thus enhancing the overall heat transfer performance. Zhao and Chen [13] use a similar concept to explain improved heat transfer from a surface consisting of microchannels in which the walls are made of compacted sintered copper particles. In their study, samples with wider microchannels display higher dryout heat fluxes. Li et al. and Li and Peterson [15,16] stress the importance of good thermal contact of the porous wick medium with the heated base and the resulting high effective thermal conductivity. In their study, wicks consisting of multiple layers of sintered copper mesh displayed high boiling dryout heat fluxes as high as 370 W/cm^2 and heat transfer coefficients as high as 25 W/cm^2-K. The dryout heat flux increased with wick thickness.

The present study implements designed biporous structures to simultaneously increase the heat dissipation capacity as well as the heat transfer coefficient of the evaporator wick. In order to avoid point contact between particles, establish greater control over porosity and pore size, and allow for a more systematic investigation of the performance, we use silicon wick structures composed of pin fin arrays periodically separated by large microchannels. These structures are developed using standard microfabrication techniques. We use these microporous structures in order

to increase capillary pressure and surface area for evaporation, as well as to reduce the maximum thickness of liquid film through which conduction occurs at the liquid–vapor interface near the meniscus. We quantitatively measure the heat transfer performance in the evaporative and nucleate boiling regimes to identify the optimum wick parameters, such as pin fin characteristic size, pin fin spacing, wick height, and microchannel width for a given wick porosity. Furthermore, applicability of these geometries to amelioration of hotspot cooling in microprocessors is examined by considering heat sources of varying area.

2 Material and Methods

2.1 Parameter Range. As illustrated in Fig. 2(*a*), the wicks of depth H are fabricated in the form of parallel microchannels of width w that periodically separate arrays of micro pin fins. The pin fins of square cross section and size d (throughout the text we denote this size d as "diameter d") and spacing p are arranged in an in-line array of width D. Table 1 shows the parameter space over which the experiments are performed. Pin fin array width D is varied from ~150 μm to ~290 μm in order to maintain the same porosity among samples ($\phi \approx 0.79 \pm 0.02$). This is done so that the effective thermal resistance of the solid pin fin wick R_{pins}, and the bulk liquid thermal resistance R_L in Fig. 2(*b*) are approximately constant among samples of similar depth H. In addition, samples are made so that the wick substrate thermal resistance $R_{substrate}$ in Fig. 2(*b*) is not the dominant resistance in the network. In this way, by varying the size and thus the surface area of the pin fins it is possible to determine how the thin liquid film thermal resistance R_{film} affects the overall performance of the wick. To
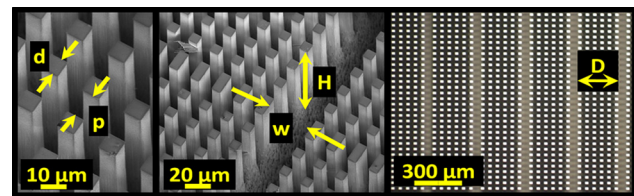
(*a*)
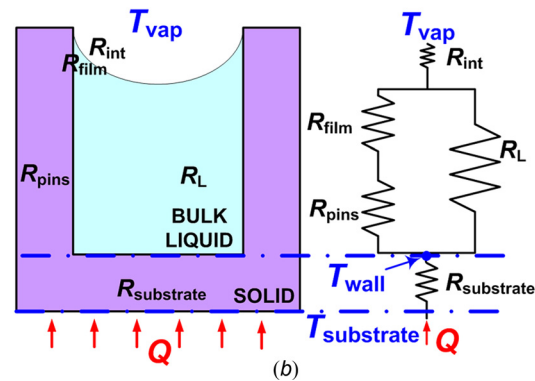
(*b*)

Fig. 2 (*a*) Cross section and plan views of the evaporator geometry showing arrays of pin fins with periodic microchannels; here d is the side length of a pin of square cross section, p is the pin spacing, H is the depth of the wick, w is the channel width, and D is the width of the pin fin array; (*b*) heat flow path and the corresponding thermal resistance network for the silicon wick structures investigated here: Q is the applied power, T_{wall} is the temperature at the base of the pin fin array, $T_{substrate}$ is the measured substrate temperature, $R_{substrate}$ is the thermal resistance of the substrate from which the pins are protruding, R_{pins} is the thermal resistance of the pin array, R_L is the bulk liquid resistance which fills the pores, R_{film} is the resistance of the liquid thin film that forms at the meniscus, R_{int} is the thermal resistance of the liquid/vapor interface, and T_{vap} is the vapor temperature

Pin fin array width D	Microchannel width w	Pin fin diameter d	Pore size p	Wick depth H
156	30	3.1	4.9	135
152	30	6.9	9.2	145
144	31	13.5	16.5	56, 145, 207, 243
232	61	7.1	8.5	150
272	61	15	16.8	149
264	61	22.5	24	152
288	61	29	28	158

arrive at values for the pin fin diameter d and pore size p, we note that the thermal resistance of a 5 μm-thick planar layer of water is ~0.074 cm^2-K/W (approximate value for the desired performance of the wick). By choosing the pore size p to vary from 28 μm down to 4.9 μm, we can generate a range of meniscus film thicknesses that yield thermal conductances in the range of the desired performance.

2.2 Sample Preparation. Figure 3 illustrates the process used to fabricate test samples on a 100 mm diameter (525 μm thick) silicon wafer. Photolithography using positive photoresist is used to define regular pin fin array patterns over a 2×2 cm^2 area. Subsequently, deep trenches are etched in the wafer using induc-
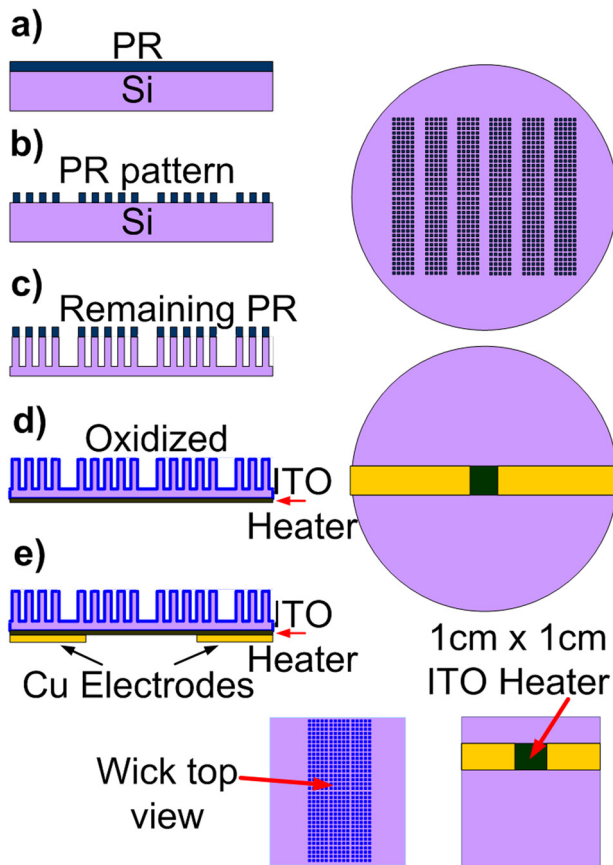

Fig. 3 Schematic of fabrication process used to generate the evaporator wick geometries: (*a*) Photoresist (PR) is deposited. (*b*) Lithography is used to define and develop the pattern. (*c*) Deep silicon etching is used to obtain a wick of desired depth. (*d*) After cleaning, the sample is oxidized to improve wettability and an ITO heater is deposited subsequently. (*e*) Copper electrodes are deposited and the sample is cut to a desired size.

tively coupled SF$_6$ plasma (Figs. 3(*a*)–3(*c*)). The photoresist is then removed by immersion in photoresist stripper (FujiFilm PRS3000) and cleaned with piranha and de-ionized water. A thin silicon dioxide layer is deposited on the wafer in order to increase wettability. This is achieved by plasma-enhanced chemical vapor deposition in oxygen plasma at 350 °C. Ellipsometry is used to measure the film thickness at the base of the microchannels of the pin fin array. The nominal measured thickness across samples is approximately 200 nm. This yielded an average contact angle of 12 ± 2.5 deg measured by a Kruss goniometer among different samples in contact with deionized water (DI^C) water. The oxide thickness is not measured along the side of the pins, but energy-dispersive X-ray spectroscopy is performed to confirm the presence of oxide at multiple locations along the pins. Resistive heating is accomplished by depositing a thin ~250 nm layer of indium tin oxide (ITO) on the back side of the silicon substrate. Lithography is used to define the heater area of 1 cm^2 (Fig. 3(*d*)), and ITO is deposited using a radio frequency argon plasma sputtering chamber. A similar process is used to deposit ~1.5 μm of copper, overlapping the edge of the ITO heater, which defines the electrodes. An array of three special limit of error Omega Engineering T-type thermocouples spaced ~2 mm apart are bonded to the heater using electrically insulating epoxy ($k_{\text{epoxy}} \approx 2.0$ W/m-K).

3 Experimental

3.1 Experimental Setup. Figure 4 shows a schematic of the experimental system for measurement of wick performance. In order to ensure that the wick is not flooded with liquid, but draws up only as much liquid as necessary to maintain it wetted, the experiments are performed with the wick suspended in a vertical orientation. The test sample is immersed in a liquid reservoir (labeled A in Fig. 4) such that the bottom edge of the ITO heater is 5 mm above the reservoir liquid level. The reservoir is replenished by liquid supply from another beaker (B) in which water is maintained at ~100 °C. The temperature of the reservoir is kept constant by immersing the reservoir in a tank (C) maintained at ~100 °C by a hot plate as well as immersed cartridge heaters. The liquid level in the reservoir is maintained by using an overflow system.

To replicate the saturation conditions in a vapor chamber heat pipe, experiments are conducted in a saturated water vapor environment at $T_{\text{sat}} \approx 100$ °C and $P_{\text{sat}} \approx 1$ bar. This is achieved by evacuating the test chamber multiple times, sealing it, and boiling the water from the overflow tank to evaporate until the chamber pressure is close to 1 bar. Thermocouples monitor the temperatures at
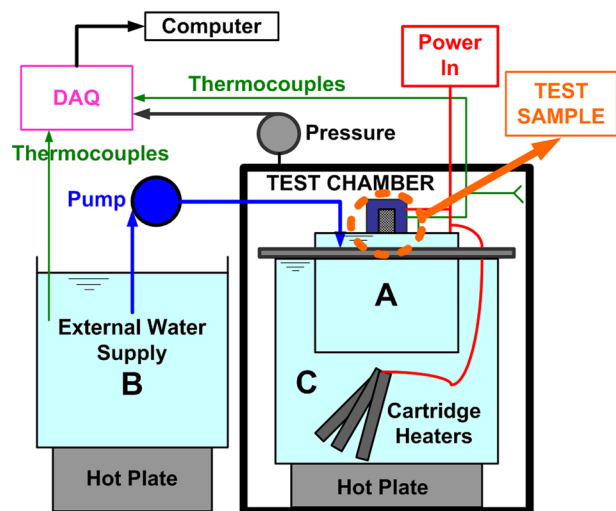

Fig. 4 Experimental apparatus used to measure the heat transfer performance of the evaporator wicks

multiple locations near the wick sample surface, in the water reservoirs, and in the vapor atmosphere as illustrated in Fig. 4. Typically, the temperature everywhere inside the chamber attains a value between 96 °C and 100 °C after 6 cycles of pumping out the chamber. This is an indication that the chamber atmosphere consists mainly of water vapor. Electrical power is then applied via a power meter (Agilent N5750A DC Power Supply—150 V/5 A/750 W) at regular intervals to the ITO heater while simultaneously measuring temperature at various points along the height of the sample. Vapor is allowed to bleed out of the system through a one-way valve in order to maintain a constant pressure.

From these experiments, we extract the heat transfer coefficient based on the heater area as follows:

$$h = \frac{Q/A_{\text{heater}}}{T_{\text{wall}} - T_{\text{vap}}} \tag{1}$$

Here, T_{wall} is the wall temperature at the wick base in contact with the liquid, T_{vap} is the saturation temperature of water vapor at ~1 bar ($T_{\text{vap}} \approx 100$ °C), A_{heater} is 1 cm^2 in all tests except when otherwise specified, and Q is the power dissipated by phase change heat transfer.

3.2 Uncertainty and Error Analysis. The primary error in measurement of heat transfer coefficient arises from uncertainty in temperature measurement and estimation of the heat losses to the ambient through nonevaporative heat transfer. The dominant mode of heat loss from the test sample is by conduction from the heater through the silicon wick substrate to the liquid reservoir. To estimate this, experiments are performed with a bare silicon surface with no wick structure and of the same dimensions as all other test samples, with power input and wick surface temperature measured as before. The power input to these bare samples reflects the losses associated with conduction through the wafer into the liquid reservoir, as well as radiation and convection heat transfer to the ambient at each measured substrate temperature. A schematic of the prepared test sample and a corresponding thermal resistance network are shown in Fig. 5. For a typical epoxy thickness of $t_{\text{epoxy}} = 3$ mm covering the back of the sample and a conservative estimate of the free convection heat transfer coefficient $h_{\text{conv}} = 0.01$ W/cm^2-K over a 1 cm^2 area, the corresponding resistances turn out to be $R_{\text{epoxy}} = 15$ cm^2-K/W and $R_{\text{conv}} = 100$ cm^2-K/W. Therefore, the high evaporative/boiling thermal resistance of the wick always measured to be less than 0.5 cm^2-K/W, and a high thermal resistance through the back side indicate that the heat lost through the back surface is no more than 1% of the input power for all the samples measured. Figure 5 also illustrates
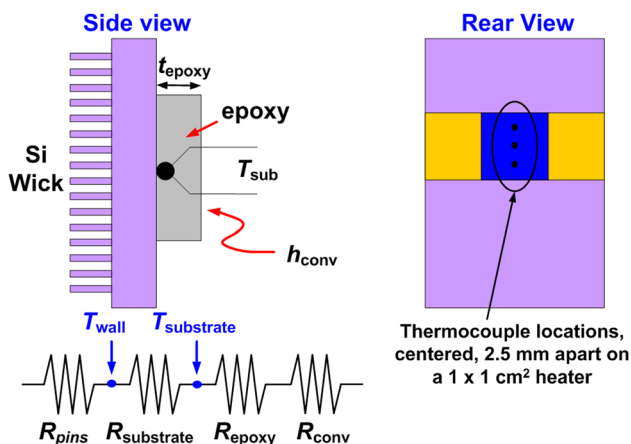

Side view   **Rear View**

Fig. 5 Sketch of resistances to heat flow generated at the back surface of the wick and the placement of the thermocouples for the wall temperature measurement

the placement of the thermocouples on the sample heater used to measure the average substrate temperature $T_{\text{substrate}}$. From experimentally obtained results, the overall heat loss Q_{loss} is correlated as a function of the substrate temperature as

$$
\begin{aligned}
Q_{\text{loss}}(W) = &-4.5 * 10^{-5}(T_{\text{substrate}} - 100)^3 \\
&+ 3.5 * 10^{-3}(T_{\text{substrate}} - 100)^2 \\
&+ 3.32 * 10^{-2}(T_{\text{substrate}} - 100) + 6.16 * 10^{-1}
\end{aligned} \tag{2}
$$

For the highest measured temperatures of 130 °C in the experiments, this value is about 3.5 W which is less than 3% of the peak heat flow through the samples with a 1 cm^2 heater size. Thus, the net power dissipated by phase change heat transfer is

$$Q = Q_{\text{inp}} - Q_{\text{loss}} \tag{3}$$

where Q_{inp} is the electrical power applied to each sample. Here Q_{inp} is also adjusted for the power dissipated in the leads that connect the samples to the power supply.

For all measured samples, we implement standard procedures for uncertainty propagation [17], where the uncertainty in a calculated quantity S is given by

$$U_S = \sqrt{\sum_1^N \left(\left(\frac{\partial S}{\partial a_i} \right) U_{a_i} \right)^2} \tag{4}$$

Here S is a calculated parameter, U_S is the uncertainty in S, a_i is a measured parameter, and U_{ai} is the uncertainty in parameter a_i. Based on standard procedures in linear regression analysis for estimating the error in slope and intercept of Eq. (2), the uncertainty in estimating the heat loss (dQ_{loss}) is about 0.2 W for values of $T_{\text{substrate}} = 130$ °C. The measured heat flux is defined as $q = Q/A_{\text{heater}}$. For large heat fluxes, $q > 100$ W/cm^2 which are of particular interest, the total uncertainty in the heat flux measurement including uncertainty in heater area and heat losses is less than 3.9% for all samples with 1 cm^2 heaters.

In order to obtain the heat transfer coefficient of the wick, the temperature at the base of the wick T_{wall} is calculated by accounting for the temperature drop through the silicon wafer using a one dimensional conduction model to yield

$$T_{\text{wall}} = T_{\text{substrate}} - q(t_{\text{wafer}} - H)/k_{\text{Si}} \tag{5}$$

Thus T_{wall} is defined in terms of the measured substrate temperature $T_{\text{substrate}}$, the total heat flux q corrected for heat losses, the overall wafer thickness t_{wafer}, the wick height H, and the thermal conductivity of silicon k_{Si}. The manufacturer-specified uncertainty in temperature measurement of the thermocouple is 0.6 K. The uncertainty in the temperature drop through the substrate is 3.1% of its value. At the highest heat fluxes, this drop can be up to 5.4 K, leading to uncertainties of 0.16 K. The total uncertainty in T_{wall} remains dominated by the manufacturer-specified uncertainty. The total measurement uncertainty in the heat transfer coefficient from Eq. (4) from a single sample is estimated using Eq. (1). This ranges from values of no more than 12.2% at low superheats (~5 K) to no more than 9.5% at high superheats (>15 K) for all samples with 1 cm^2 heaters.

To verify the assumptions used in the uncertainty estimates, a finite element calculation is performed for representative values of power and temperature observed in the experiment. A rectangular plate of silicon, with area of 2×2 cm^2 and of thickness 525 μm is considered representing the entire sample containing the wick and substrate. The central area of 1×1 cm^2 on one side of the wafer has an imposed heat flux of 100 W/cm^2, while a heat transfer coefficient of 12 W/cm^2-K is imposed resembling a measured evaporative heat transfer on the coinciding central area on the other side containing the wick. Additional boundary conditions are chosen so
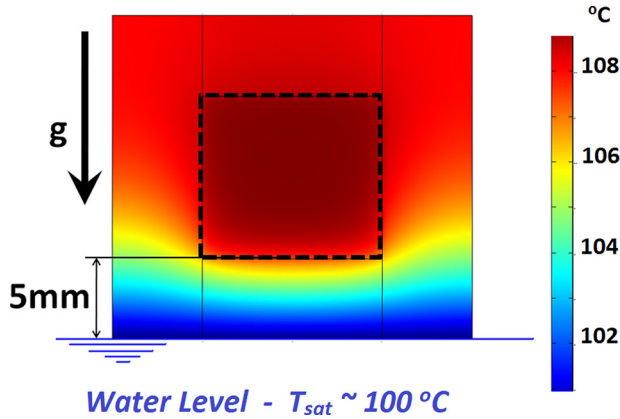
Fig. 6 Temperature contours (in °C) from finite element analysis for an imposed heat flux of 100 W/cm² and evaporation coefficient of 12 W/cm²-K. Here one end of wafer is assumed to be at the saturation temperature of water $T_{sat} = 100\,°C$. Black dashed line indicates relative size of the 1×1 cm² heater centered on a 2×2 cm² wick. These contours represent the measured substrate temperature field $T_{substrate}$.

that one end face of the plate of dimensions 2 cm × 525 μm is assumed to be maintained at $100\,°C$ representing immersion in the large liquid reservoir. A free convection heat transfer coefficient of $h_{conv} = 0.01$ W/cm²-K is imposed on all other faces of the plate for heat exchange with the ambient which is assumed to be at $100\,°C$. Figure 6 presents temperature contours on the substrate side of the wafer where $T_{substrate}$ is measured. A sharp temperature gradient is observed on one side of the wafer, which corresponds to conduction away from the wick area towards the liquid pool. Numerical integration of the resultant heat flux yields an overall heat loss of $\sim$3.2 W (3.2% heat loss), which compares well with measured heat losses from bare silicon samples[1].

4 Results and Discussion

4.1 Effect of Wick Depth on Performance: Predominantly Evaporative Regime. Wick samples are tested in a vertical orientation as depicted in Fig. 4. When water saturates the wick, the thermal resistance of the bulk liquid R_L between the pins as seen in Fig. 2(b) is roughly two orders of magnitude higher than the resistance through the silicon pins R_{pins}. Therefore, most of the heat travels through the solid substrate and the pin structures to the thin liquid film that forms at the meniscus where the bulk of the evaporative heat transfer occurs. With these considerations in mind, the resistance network in Fig. 2(b) can be simplified as a series network with R_L omitted and including the substrate, pin fin array, thin liquid film, and interfacial thermal resistances designated as $R_{substrate}$, R_{pins}, R_{film}, and R_{int}, respectively. Furthermore, if we only consider the thermal resistances in the pin fin array of the wick of 1 cm² area we obtain

$$\frac{1}{g_{pins}} = \frac{H}{(1 - \phi)k_{Si}} \qquad (6)$$

where the term on the right hand side is the thermal resistance of the pin fin array R_{pins}. Here, H is the depth of the pin array, ϕ the porosity, k_{Si} the thermal conductivity of silicon at $115\,°C$, and

---

[1]The overall heat loss due to spreading estimated by Eq. (3) and supported by the finite element models are accounted for in all presented data. In this way, we are able to isolate the total heat flux that is dissipated by evaporation/boiling within some uncertainty. Therefore, even though we cannot determine quantitatively the total area over which the bulk of the evaporation/boiling occurs, we can estimate the temperature T_{wall} at the pin fin array base using Eq. (5). This way of defining the heat transfer coefficient includes the lateral heat spreading in the samples dissipated by evaporation/boiling.

g_{pins} is the thermal conductance of the pin fin array. As channel depth is increased from $H = 56$ μm to $H = 243$ μm in experiments considered here, the conductance of the solid pins with porosity $\phi \sim 0.79$ drops from $g_{pins} = 1/R_{pins} = 43.2$ W/cm²-K down to $g_{pins} = 9.9$ W/cm²-K. For the range of pore sizes investigated here, the effective liquid film thickness at the meniscus has been estimated by several investigators to be under 5 μm [9,18], giving a thin film conductance to be $g_{film} = 1/R_{film} = 13.6$ W/cm²-K. Therefore, pin fin arrays deeper than 145 μm ($g_{pins} = 1/R_{pins}$ < 15.9 W/cm²-K) contribute the dominant thermal resistance. This implies that in the range of depths considered here, a transition is likely to occur in the thermal resistances that dominate (between R_{film} and R_{pins}) and thus yield different trends in heat transfer performance among samples investigated.

Figure 8(a) shows the effect of varying the depth H of the micro pin fin structures on wick performance for the case $d = 13.5$ μm, $p = 16.5$ μm, $w = 31\mu$m and porosity $\phi \sim 0.79$. Predominantly evaporative heat transfer is observed only in wicks of depth $H = 145$ μm and below. Here we presume that bubble nucleation at the measured temperatures is suppressed due to high wettability of water on SiO₂ precluding vapor trapping [19]. For these samples, the pin array conductance estimated by Eq. (6) (g_{pins} > 15.9 W/cm²-K) remains comparable or larger than the liquid film conductance g_{film}. In this scenario, the film conductance governs the heat transfer and the initial slope of the curves remains independent of wick depth (similar slopes for $H = 56$ μm and $H = 145$ μm).

At low to moderate heat fluxes, when the wick is saturated with liquid (Fig. 7), the liquid film conductance g_{film} is a function of thin liquid film thickness and the total length of the contact line, i.e., the total area of the thin liquid film surrounding the pin. As the applied heat flux and mass flow rate increase, the capillary limit is reached near the center of the heater and local dryout occurs evinced by a visible dry spot on the wick surface. We conjecture that there must be a radial variation of the liquid level away from the dry spot, rising from zero at the edge of the spot to the top of the pin fins far away from the spot, as depicted in Fig. 7. As a result, the effective area of thin film is significantly enhanced just prior to dryout, with evaporation occurring in the thin film around the pin fins as well as from the base on which the pin fins stand. In addition, at high heat fluxes the contact angle is at the minimum possible value, the receding contact angle for water on SiO₂. It is possible that this recession further thins down the liquid film where the bulk of the evaporation occurs, and slightly increases the film thermal conductance. We presume that these two effects working in tandem increase the slope at high heat fluxes, most clearly apparent for q > 90 W/cm² in a wick of $H = 145$ μm (Fig. 8(a)), and translate into a higher heat transfer coefficient (Fig. 8(b)). Once observed the dry spot remains stable and gradually grows to cover up to about 10% of the heater area. Further increase in heat flux causes the dry spot to spread dramatically and blanket the whole surface of the wick with vapor. We deem this as the dryout heat flux and observe a sudden increase in average superheat. At this point the wick can no longer be
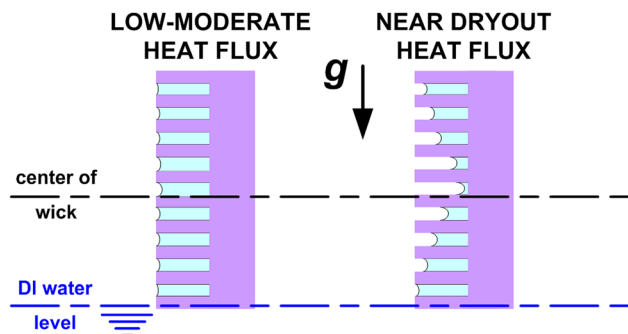

Fig. 7 Sketch of the wick and liquid level based on experimental observations at low to moderate and high heat fluxes
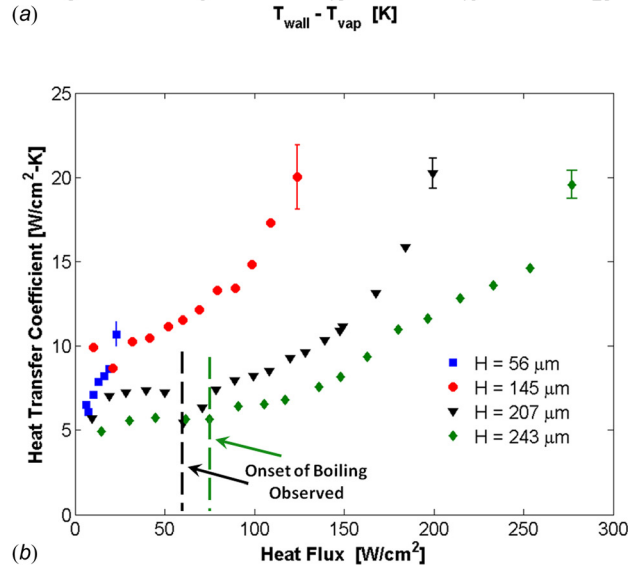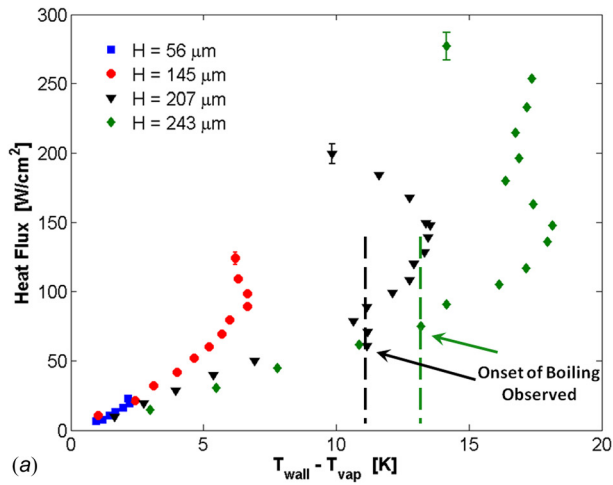

Fig. 8 (*a*) Heat transfer data for pin fin arrays of variable depth *H*, for constant pin fin size *d* = 13.5 μm, pore size *p* = 16.5 μm, pin array width *w* = 144 μm, and microchannel width *w* = 31 μm. (*b*) Heat transfer coefficient variation with wick depth *H*. Only error bars at dryout heat fluxes are shown for each data set.

considered operational. In most samples, we observe the dry spot to occur and be stable within 10–15% of the dryout heat flux. The dryout condition corresponds to the last data point for each sample plotted in Figs. 8(*a*) and 8(*b*). From these experiments we observe

that in the predominantly evaporative regime of heat transfer, dry-out occurs at larger values of applied heat flux as the pin fin height is increased from 56 μm to 145 μm, presumably due to the increased cross-sectional area available for flow through the taller microchannels.

4.2 Effect of Wick Depth on Performance: Predominantly Boiling Regime. As the wick depth *H* is increased beyond 145 μm, the conductance of the pin array g_{pins} decreases (see Eq. (6)) and is lower than the liquid film conductance g_{film}. The initial slope of the heat transfer curve becomes a function of the pin fin height, as seen in Fig. 8(*a*) for *H* = 207 μm and *H* = 243 μm. Consequently, high values of superheat are observed at relatively low heat fluxes (∼50 W/cm²). Here, nucleate boiling is visually observed at several locations on the wick as indicated by the dotted lines in Figs. 8(*a*) and 8(*b*). For samples that demonstrate nucleate boiling, the heat transfer curve has two distinct slopes: one corresponding to predominantly evaporation at low to moderate heat fluxes, and another corresponding to predominantly nucleate boiling at high heat fluxes. The slope of the heat transfer curve in the nucleate boiling regime is increased due to enhanced thin film area caused by ebullition of the generated bubbles. Escaping bubbles are constrained in the lateral direction and elongated along the pores of the wick. This creates a thin film along the height of the pin fin instead of only near the meniscus as in evaporation. The thickness of the film on the sides of the pins depends on the bubble velocity and the pore size [20,21]. While it is generally observed that boiling in microchannel based heat pipes causes flow blockage and stops heat pipe operation, in the present study, a steady boiling regime could be maintained for heat flux increases up to 185 W/cm² beyond nucleation incipience for 1 cm² heaters. The occurrence of nucleate boiling in biporous particle structures and layered meshes has been previously shown to yield high-performance wicks [12–15]. The structure and dynamics of the flow have remained a matter of conjecture. In this study, we supplement the heat transfer measurements with flow visualization of a stable nucleate boiling regime that is observed.

The visualization of boiling in wick structures is performed outside the test chamber using a Fastec Imaging (IN100M2GB) CCD camera. Images are taken at 250 frames per second. Figure 9 shows the boiling process for a wick of depth *H* = 207 μm, with *d* = 13.5 μm pin fins, *p* = 16.5 μm pore size, and *w* = 31 μm microchannels. At a heat flux of 52 W/cm², bubble nucleation occurs in the microchannels (Fig. 9(*a*)), with the bubbles typically growing to a diameter equaling the combined width of two pin fin arrays (∼350 μm) before collapsing. As the heat flux is increased to 107 W/cm², the superheat increases. Bubbles nucleating in microchannels collapse at smaller sizes, while nucleation also
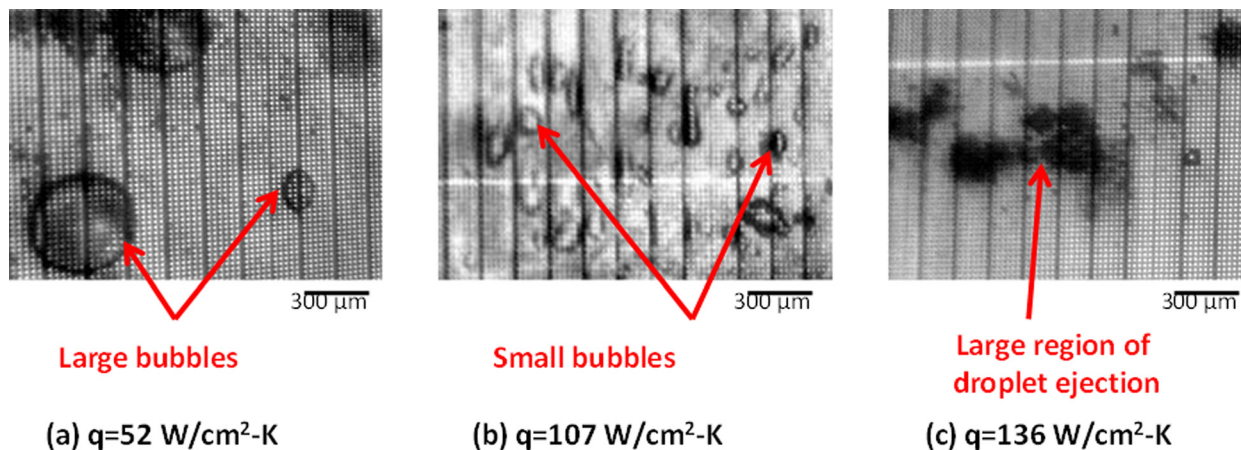

(a) q=52 W/cm²-K   (b) q=107 W/cm²-K   (c) q=136 W/cm²-K

Fig. 9 Images of nucleate boiling at various heat fluxes in a wick sample for *d* = 13.5 μm, *p* = 16.5 μm, *H* = 207 μm, and *w* = 30 μm

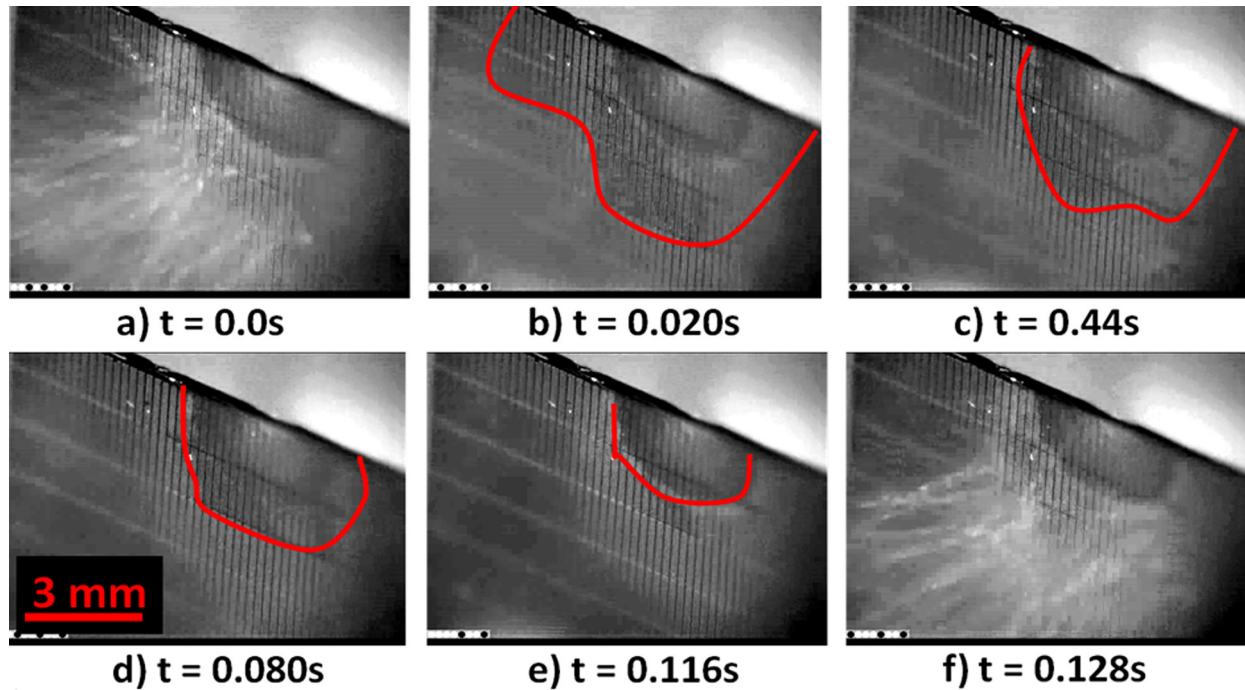**Fig. 10 Burst sequence at an imposed heat flux of ~230 W/cm^2: (a) Bubble bursting and violent ejection of liquid droplets. (b) Formation of dry area around nucleation site. (c) and (d) Advancing wetting front. (e) Liquid almost fully rewetting the wick. (f) Start of next burst cycle.**

occurs in the smaller pores formed by the pin fins (Fig. 9(b)). In actual experiments, these bubbles appear and disappear very rapidly (~0.01 s). As the heat flux is further increased to 136 W/cm^2, the frequency of bubble generation increases. Bubbles are intermittently formed at discrete nucleation sites on the wick surface, and collapse when they grow beyond the wick height. In addition to these discrete locations, large areas in the pin fin array are seen to nucleate simultaneously (large dark spots in Fig. 9(c)), resulting in audible loud bursting and violent ejection of liquid droplets. This bursting phenomenon causes the slope of the data to increase abruptly or even become negative giving a significant increase in heat transfer coefficient that causes a reduction in average superheat. This is evident in Fig. 8(a) for the wicks of depth $H = 207$ μm and $H = 243$ μm, at average values of superheat of ~13 K and ~18 K, respectively, where this bursting phenomenon is initially observed. This phenomenon commences at a larger average superheat than that corresponding to the isolated bubble nucleation indicated by the dashed lines in Fig. 8.

Figures 10(a)–10(f) shows one such cycle of bursting and receding of the wetting front followed by advancement of the wetting front back towards the nucleation zone. Immediately after droplet ejection, a large dry area is formed as seen in Fig. 10(a). In subsequent frames (Figs. 10(b)–10(e)) motion of the liquid–vapor–solid contact line can be discerned, indicating liquid flow towards the nucleation area and rewetting of the surface, until the next burst occurs (Fig. 10(f)). This process of rewetting shows that capillary pumping continues to be active even after the onset of nucleate boiling, and indicates that this regime of bubble nucleation is not an operating limit in such biporous structures. To the best of our knowledge, this regime of stable boiling has not yet been visually observed in other thin liquid film wick structures. As the heat flux is increased, the ejection frequency increases and the motion of the front can no longer be seen. At this point, the bubble ejection frequency is very high and the area where the nucleation occurs is so large that the wick can no longer supply the liquid to the surface. Here, the boiling limit is reached and the wick dries out.

4.3 Effect of Wick/Heater Area Ratio on Performance. As the applied heat flux is increased, the capillary pressure increases

in order to accommodate for the increased rate of evaporation [5]. This process induces entrainment of liquid towards the area directly above the heater, where the surrounding region acts as a liquid reservoir. Therefore, for a given wick structure, the ratio of the total wick area to the heater area influences the dryout heat flux. The area over which evaporation occurs is difficult to determine visually; investigators usually resort to rough approximations for the evaporation area [10] or report the applied heat flux based on the heater area [22,23]. Figure 11 shows a sketch of the general arrangement of the heater area (on the back of the wafer) within the wick. In one case, the wick dimensions above the reservoir liquid level are 1.9×2 cm^2, with the 1 cm^2 heater aligned centrally within the wick and with the reservoir level 5 mm below the heater edge. In another case, the wick area is 1×1.5 cm^2, and is aligned on three sides with the 1 cm^2 heater. Figure 12 shows the effect of this difference in wick and heater area on the wick performance. All data presented in Fig. 12 are for a single wick geometry with pin fin size $d = 7.1$ μm, pore size $p = 9.0$ μm, channel width $w = 30$ μm, and wick depth $H \approx 149$ μm. The larger area of the wick in the second case yields an improved dryout flux of 119.6 ($\pm$4.2) W/cm^2 compared to 73.6 ($\pm$2.6) W/cm^2 for the first case. The heat transfer coefficient also increases from 9.8 ($\pm$0.7) W/cm^2-K to 13.4 ($\pm$1.5) W/cm^2-K at a heat flux of approximately 60 W/cm^2 due to an increase in the effective contact line length for evaporation in the larger wick. The data
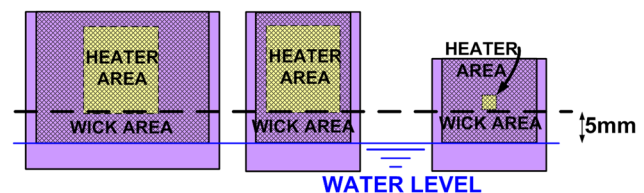

Fig. 11 Sketch of arrangement of wick and heater surfaces with respect to the liquid reservoir: (a) $A_{wick} = 3.8$ cm^2, $A_{heater} = 1$ cm^2 (b) $A_{wick} = 1.5$ cm^2, $A_{heater} = 1$ cm^2 and (c) $A_{wick} = 1.1$ cm^2, $A_{heater} = 0.0625$ cm^2

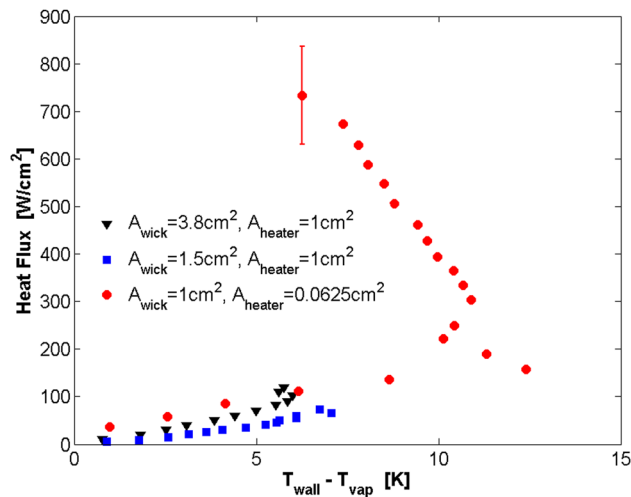**Fig. 12 Effect of the ratio of wick surface area to heater area, for $d = 7.1$ μm, $p = 9.0$ μm, $w = 30$ μm, and $H = 149$ μm. Only the error bar at dryout heat flux is shown for each data set, where the two sets with lower attained heat fluxes have error bars that are smaller than the marker size.**

suggests that larger wick-to-heater area ratios ought to allow for higher heat fluxes to be dissipated, since cooler liquid from the surrounding areas can penetrate deeper into the central hotspot before evaporating. This has particular relevance to the cooling of local hotspots within a microprocessor, where high heat fluxes on the order of hundreds of W/cm^2 may be generated [1–3]. In order to simulate a single hot spot on a chip, we fabricated a 2.4 mm × 2.6 mm heater on a 1.1 cm^2 wick for an area ratio of about 18:1 (filled red circles in Fig. 12). For this heater size, evaporation predominates for heat fluxes as high as ∼160 W/cm^2 beyond which nucleate boiling occurs until the dryout flux of 733.1 (± 103.4) W/cm^2 is reached. With this performance, thermal non-uniformities that may arise over small areas (on the order ∼1 mm^2 or less) of a microprocessor chip [1,2] can be managed. This effect may also explain the high dryout fluxes (∼600 W/cm^2) observed by other investigators [22,23] for area ratios of approximately 25:1 and 16:1, respectively.

4.4 Effect of Pin/Pore Size on Performance. Wayner and co-workers [24,25] have shown that in the microscale region of the liquid film near the wall consists of: (a) a nonevaporating film where long range intermolecular forces suppress evaporation, (b) a region of constant curvature where surface tension is dominant, and (c) an interline region where both surface tension and intermolecular forces are important. In the interline region (length–several hundred nm) high mass (heat) fluxes occur due to enhanced fluid flow towards the contact line, modifying the film profile and the apparent contact angle [26]. However, this region occupies a small fraction of the total film length for large menisci (radius > few μm). Therefore, the major portion of the heat transfer occurs through conduction in the microscale liquid film (thickness∼few μm) of constant curvature [18,27,28]. In order to increase total heat flux, one needs to increase the number of such regions by reducing pore size.

Figures 13(a) and 13(b) show the effect of varying the pin fin size d and spacing p on the heat transfer curve, for channel depths H in the range between 135 μm and 158 μm as summarized in Table 1, and channel widths w of 30 μm and 60 μm. Expectedly, from Fig. 13(b) it is evident that for samples with $w \approx 60$ μm, the heat transfer coefficient increases as pore size p decreases from 28 μm to 8.5 μm because in this manner the number of pins and thus available area for evaporation of thin liquid film near the contact line is increased. In samples with $w \approx 30$ μm, there is an increase in heat transfer coefficient as pore size p is decreased
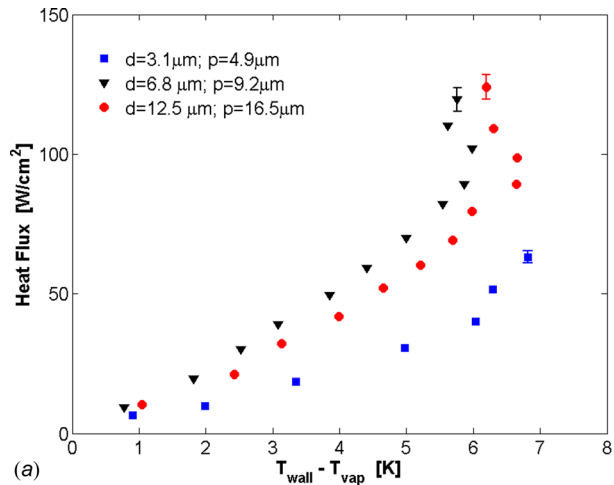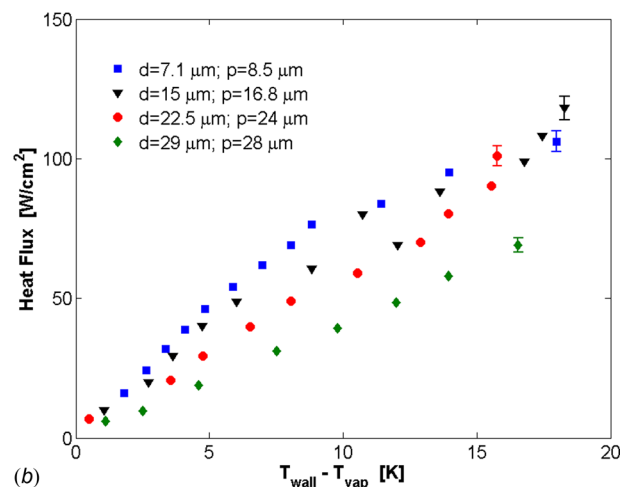
Fig. 13 (a) Heat transfer data for various pin fin and pore size with channel size $w = 30$ μm, nominal array width $D = 150$ μm, and nominal wick depth $H = 145$ μm. (b) Heat transfer data for varied pin fin size with channel size $w = 60$ μm, nominal array width $D = 260$ μm, and nominal depth $H = 150$ μm. Only error bars at dryout heat fluxes are shown for each data set.

from 16.5 μm to 9.2 μm. For $p = 9.2$ μm, the heat transfer coefficient reaches a maximum of 20.7 (±2.4) W/cm^2-K at a dryout heat flux of 119.6 (±4.2) W/cm^2. For large (∼1cm^2) heaters, this represents both the highest heat flux and the highest heat transfer coefficient reported in literature for the predominantly evaporative heat transfer attesting to the benefits of using biporous wick structures. The heat transfer coefficient drops significantly for the smallest pore size of $p = 4.9$ μm which might entail a different physical explanation deviant from expectation as detailed below.

For a scaling analysis valid to leading order, we neglect spatial variations in curvature, all convective effects, and approximate the region of dominant thermal resistance as a thin liquid film of height L_{film} and average thickness δ near the top of each pin (Fig. 14). The dominance of conduction over convection in the pores of the wick is verified by considering the Peclet number vd/α. Here v is the velocity of liquid required to maintain a fixed liquid/vapor interface undergoing evaporation, d is the characteristic length scale which in this case is the pin size, and α is the liquid thermal diffusivity. The velocity is calculated by

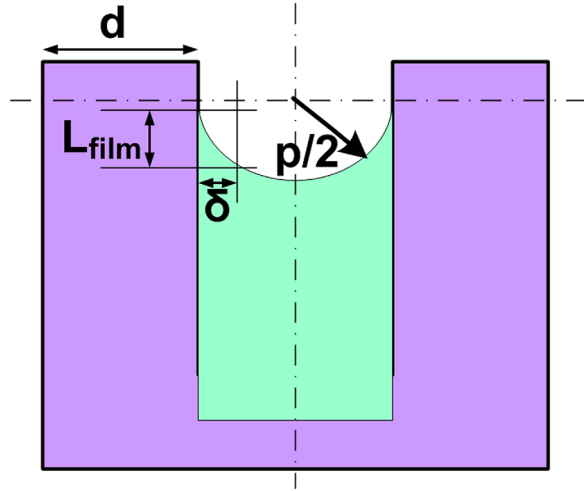$$v = \frac{q}{\rho_l h_{fg}} \tag{7}$$

Fig. 14 Sketch of a thin liquid film and meniscus around a micro pin fin. Here L_{film} is the liquid film length along the pin that forms at the meniscus, p is the pore size spanning the pins, d is the side length of a square cross section pin, and δ is the thickness of the thin liquid film.

Fig. 15 Variation of the thermal conductance of the thin liquid film as a function of pore size at moderate evaporative heat fluxes of $\sim$60 W/cm^2

For the highest levels of heat flux considered of approximately $q = 200$ W/cm^2, this velocity scale is on the order of $v \approx 1$ mm/s which yields Peclet numbers that range from 1.7×10^{-2} for the smallest pin size tested $d = 3.1$ μm to 1.59×10^{-1} for $d = 29$ μm. This implies that even at such high heat fluxes, conduction heat transfer is still the dominant mode by at least one order of magnitude.

In the wick structures considered here composed of pin fins with square cross section and side length d and pin spacing p, the length L_{film} of the thin liquid film near the contact line is truncated by the assumed constraint that the meniscus takes on a spherical shape away from the solid surface and perfectly wets the solid surface (Fig. 14). The number of pins N protruding out of an area A is $N = (1 - \phi)A/d^2$. Thus, the conductance (W/cm^2-K) of the liquid film is

$$g_{film} = \frac{(1 - \phi)}{d^2} \frac{k_l(4d)L_{film}}{\delta} \qquad (8)$$

where $(4d)L_{film}$ is the surface area of the thin liquid film surrounding the pin of size d. Considering a two-dimensional situation (Fig. 14), the scales L_{film} and δ are related through the relation

$$L_{film} \approx \sqrt{(p/2)^2 - (p/2 - \delta)^2} \qquad (9)$$

Under this assumption, the conductance can be determined in terms of all measurable quantities with the film thickness δ being the only fitting parameter.

$$g_{film} = \frac{4k_l(1 - \phi)}{d} \sqrt{\frac{p}{\delta} - 1} \qquad (10)$$

We observe that at low to moderate heat fluxes, the slopes of the heat transfer curve are nearly independent of applied heat flux for all pore sizes. This indicates that the liquid level in the wick is high, the base of the wick structure is not activated, and the assumptions used in deriving Eq. (10) are satisfied. For comparison of the observed film conductance with the predictions of Eq. (10), we extract heat transfer coefficients from Fig. 13(a) for various pore sizes at a moderate heat flux of $\sim$60 W/cm^2 where evaporation is the dominant mode of heat transfer. A 1-D conduction model is used to extract the film conductance. This analysis assumes a heat transfer area of 1cm^2 at the base of the pins, which translates into varied thin film area as p and d are varied as indicated by $(4d)L_{film}$ term in Eq. (8). A potentially larger area for evaporation due to thermal spreading is captured in the uncer-
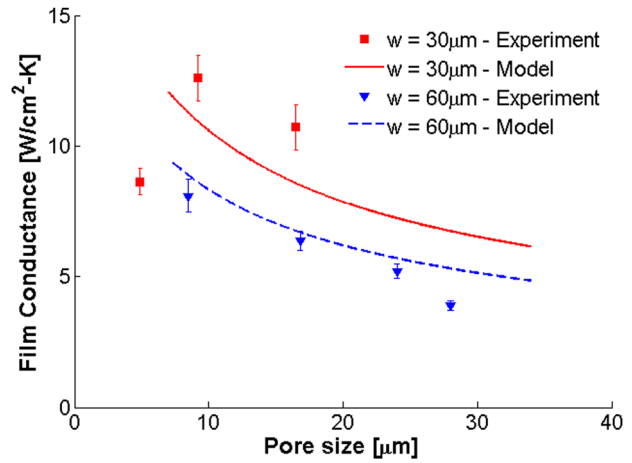
tainty and will not affect the trend with p significantly. Eq. (10) is plotted in Fig. 15 as a solid line for a film thickness $\delta = 4$ μm. The data for samples with channels $w \approx 60$ μm appear to follow the $\sqrt{p/\delta - 1}$ trend predicted by Eq. (10). A similar trend can be discerned for the samples with channels $w \approx 30$ μm (dashed line in Fig. 15, $\delta = 4$ μm), for which the values of conductance are higher for the 9.2 μm and 16.5 μm pores. The higher values of conductance for the samples with 30 μm channels are attributed to a greater wicking area around the heater of 4.2 cm^2 compared to a value of 3.8 cm^2 for those with 60 μm channels which is a consequence of the fabrication. This reduces the number of pins by roughly 10% when the larger channels are used. The only anomaly to the trend is the film conductance for the sample with $p = 4.9$ μm pores and $w = 30$ μm channel. Here the conductance dips sharply below the estimated trend. We attribute this to the suppression of evaporation caused by interface curvature and reduced liquid pressure.

To better interpret these results, we let T_1 be the temperature of bulk liquid, while the curved liquid–vapor phase interface is at T_{lv}. For the two-dimensional geometry considered here, the superheat required for phase equilibrium is given by combining the Kelvin and Clapeyron effects to yield

$$T_{lv} = T_{sat}(P_l)\left[1 + \frac{\sigma}{(p/2)\rho_v h_{fg}}\right] \qquad (11)$$

As pore size p is reduced from 16.5 down to 4.9 μm, Eq. (11) predicts the required superheat to be of the order of 1–6 K, respectively. In a situation far from equilibrium with high interfacial mass fluxes, the required superheat may be considerably larger. Consequently, as pin size d and pore size p decrease in order to increase the surface area for evaporation, a larger fraction of the heat flux from the pin fin is used to superheat the liquid flowing towards the meniscus resulting in low observed overall heat transfer coefficient for $p = 4.9$ μm. Numerical calculations by Ranjan et al. [29] indicate that increases in superheat of even 2–4 K can reduce interfacial evaporation coefficients by as much as an order of magnitude.

5 Conclusions

Experimental data are presented for evaporation from a biporous medium consisting of pin fin arrays periodically separated by larger microchannels.

1. Heat fluxes of up to 119.6 ($\pm$4.2) W/cm^2 can be dissipated in predominantly evaporation heat transfer, accompanied by heat transfer coefficients of 20.7 ($\pm$2.4) W/cm^2-K. While

the mechanism and the interplay between evaporation and boiling are not completely understood to the best of our knowledge, for heater size considered here, these values represent some of the higher heat flux dissipated in a predominantly evaporative mode of heat transfer from porous structures.

2. For larger pores and deeper wicks ($p > 16$ μm and $H > 145$ μm respectively), a nucleate boiling regime is observed with high dryout heat fluxes up to 277.0 (± 9.7) W/cm^2 for large heaters (~ 1 cm^2), and high heat transfer coefficients up to 19.6 (± 0.8) W/cm^2-K. A stable regime of boiling is observed for up to 185 W/cm^2 beyond the heat flux of boiling incipience in these samples.

3. For small heaters of area 0.0625 cm^2, high heat fluxes of up to 733.1 (± 103.4) W/cm^2 can be dissipated, making these wick structures attractive for hotspot thermal management.

4. The overall heat transfer coefficient is increased with a reduction in pore size and accompanying increase in surface area. A simple model is proposed that captures the trends in the observed data.

Acknowledgment

Nomenclature

d = pin fin diameter, m
D = width of pin fin array, m
g_{film} = conductance of liquid film, W/m^2-K
h = heat transfer coefficient, W/m^2-K
h_{conv} = free convection heat transfer coefficient, W/m^2-K
H = height of pin fins/microchannels, m
k_{epoxy} = thermal conductivity of the thermal epoxy, W/m-K
k_{Si} = thermal conductivity of silicon, W/m-K
L_{film} = length of thin film surrounding each pin fin, m
P = pressure, N/m^2
p = pore size–pin fin spacing, m
q = heat flux, W/m^2
Q = heat flow corrected for heat losses, W
Q_{inp} = heat generated via power supply, W
Q_{loss} = total measured heat loss by any means other than phase change heat transfer, W
R_{conv} = convective thermal resistance, m^2-K/W
R_{film} = thermal resistance of the liquid film, m^2-K/W
R_{int} = thermal resistance of the liquid/vapor interface, m^2-K/W
R_L = thermal resistance of the liquid filling the wick, m^2-K/W
R_{matrix} = thermal resistance of the solid liquid matrix, m^2-K/W
R_{pins} = thermal resistance of the solid pin fins of the wick, m^2-K/W
$R_{substrate}$ = thermal resistance of the substrate, m^2-K/W
t_{wafer} = thickness of the silicon wafer, m
T = temperature, K
$T_{substrate}$ = temperature of the substrate, K
T_{vap} = temperature of the vapor at saturation pressure, K
T_{wall} = temperature of the pin array base in contact with the liquid, K
U = uncertainty
v = velocity scale, m/s
w = width of microchannel, m

Greek Symbols

δ = liquid film thickness surrounding a pin fin, m
ϕ = porosity
ρ = density, kg/m^3
σ = surface tension, N/m

Subscripts

lv = liquid–vapor interface
l = liquid
sat = saturation conditions

References

[1] Mahajan, R., Chiu, C., and Chrysler, G., 2006, "Cooling a Microprocessor Chip," Proc. IEEE, **94**(8), pp. 1476–1486.
[2] Majumdar, A., 2009, "Thermoelectric Devices: Helping Chips to Keep Their Cool," Nat. Nanotechnol., **4**(4), pp. 214–215.
[3] Garimella, S. V., Fleischer, A. S., Murthy, J. Y., Keshavarzi, A., Prasher, R., Patel, C., Bhavnani, S. H., Venkatasubramanian, R., Mahajan, R., Joshi, Y., Sammakia, B., Myers, B. A, Chorosinski, L., Baelmans, M., Sathyamurthy, P., and Raad, P. E., 2008, "Thermal Challenges in Next-Generation Electronic Systems," IEEE Trans. Compon. Packag. Technol., **31**(4), pp. 801–815.
[4] Prasher, R. S., 2003, "A Simplified Conduction Based Modeling Scheme for Design Sensitivity Study of Thermal Solution Utilizing Heat Pipe and Vapor Chamber Technology," ASME J. Electron. Packag., **125**(3), pp. 378–385.
[5] Faghri, A., 1995, Heat Pipe Science and Technology, Taylor and Francis, Washington, DC.
[6] Khrustalev, D., and Faghri, A., 1995, "Heat Transfer During Evaporation on Capillary-Grooved Structures of Heat Pipes," ASME J. Heat Transfer, **117**(3), pp. 740–747.
[7] Stephan, P. C., and Busse, C. A., 1992, "Analysis of the Heat Transfer Coefficient of Grooved Heat Pipe Evaporator Walls," Int. J. Heat Mass Transfer, **35**(2), pp. 383–391.
[8] Xu, X., and Carey, V. P., 1990, "Film Evaporation From a Micro-Grooved Surface—An Approximate Heat Transfer Model and Its Comparison With Experimental Data," J. Thermophys., **4**(4), pp. 512–520.
[9] Hanlon, M. A., and Ma, H. B., 2003, "Evaporation Heat Transfer in Sintered Porous Media," ASME J. Heat Transfer, **125**(4), pp. 644–652.
[10] Davis, T. W., and Garimella, S. V., 2008, "Thermal Resistance Measurement Across a Wick Structure Using a Novel Thermosyphon Test Chamber," Exp. Heat Transfer, **21**(2), pp. 143–154.
[11] Cao, X. L., Cheng, P., and Zhao, T. S., 2002, "Experimental Study of Evaporative Heat Transfer in Sintered Copper Bidispersed Wick Structures," J. Thermophys. Heat Transfer, **16**, pp. 547–552.
[12] Semenic, T., Lin, Y., Catton, I., and Sarraf, D., 2008, "Use of Biporous Wicks to Remove High Heat Fluxes," Appl. Therm. Eng., **28**(4), pp. 278–283.
[13] Zhao, Y., and Chen, C., 2007, "Vaporization Heat Transfer in Sintered Copper Wicks With Micro-Grooves in Heat Pipe Evaporators," Thermal Challenges in Next Generation Electronic Systems, S. V. Garimella and A. S. Fleischer, eds., Millpress, Rotterdam.
[14] Liao, Q., and Zhao, T. S., 1999, "Evaporative Heat Transfer in a Capillary Structure Heated by a Grooved Block," J. Thermophys. Heat Transfer, **13**(1), pp. 126–133.
[15] Li, C., Peterson, G. P., and Wang, Y., 2006, "Evaporation/Boiling in Thin Capillary Wicks (I)—Wick Thickness Effects," ASME J. Heat Transfer, **128**(12), pp. 1312–1319.
[16] Li, C., and Peterson, G. P., 2006, "Evaporation/Boiling in Thin Capillary Wicks (II)—Effects of Volumetric Porosity and Mesh Size," ASME J. Heat Transfer, **128**(12), pp. 1320–1328.
[17] Coleman, H. W., and Steele, W. G., 1999, Experimentation and Uncertainty Analysis for Engineers, John Wiley and Sons, New York.
[18] Wang, H., Garimella, S., and Murthy, J., 2007, "Characteristics of an Evaporating Thin Film in a Microchannel," Int. J. Heat Mass Transfer, **50**(19–20), pp. 3933–3942.
[19] Dhir, V. K., 1998, "Boiling Heat Transfer," Annu. Rev. Fluid Mech., **30**(1), pp. 365–401.
[20] Bretherton, F. P., 2006, "The Motion of Long Bubbles in Tubes," J. Fluid Mech., **10**, pp. 166–188.
[21] Ajaev, V. S., and Homsy, G. M., 2006, "Modeling Shapes and Dynamics of Confined Bubbles," Annu. Rev. Fluid Mech., **38**, pp. 277–307.
[22] Cai, Q., and Chen, C.-L., 2010, "Design and Test of Carbon Nanotube Biwick Structure for High-Heat-Flux Phase Change Heat Transfer," ASME J. Heat Transfer, **132**(5), p. 052403.
[23] Weibel, J. A., Garimella S. V., and North, M. T., 2010, "Characterization of Evaporation and Boiling From Sintered Powder Wicks Fed by Capillary Action," Int. J. Heat Mass Transfer, **53**(19–20), pp. 4204–4215.
[24] Potash, M., and Wayner, P. C., 1972, "Evaporation From a Two-Dimensional Extended Meniscus," Int. J. Heat Mass Transfer, **15**(10), pp. 1851–1863.
[25] Wayner, P. C., 1999, "Intermolecular Forces in Phase-Change Heat Transfer: 1998 Kern Award Review," AIChE J., **45**(10), pp. 2055–2068.
[26] Plawsky, J., Ojha, M., Chatterjee, A., and Wayner, P., 2009, "Review of the Effects of Surface Topography, Surface Chemistry, and Fluid Physics on

Evaporation at the Contact Line," Chem. Eng. Commun., **196**(5), pp. 658–696.

[27] Morris, S. J. S., 2003, "The Evaporating Meniscus in a Channel," J. Fluid Mech., **494**, pp. 297–317.

[28] Dhavaleswarapu, H. K., Garimella, S. V., and Murthy, J. Y., 2009, "Microscale Temperature Measurements Near the Triple Line of an Evaporating Thin Liquid Film," ASME J. Heat Transfer, **131**(6), p. 061501.

[29] Ranjan, R., Murthy, J. Y., and Garimella, S. V., 2009, "Numerical Study of Evaporation Heat Transfer From the Liquid-Vapor Interface in Wick Microstructures," Proceedings of ASME-IMECE, IMECE 2009-11326, Lake Buena Vista, Nov. 13–19.